



On the north equatorial current spatiotemporal modes and responses in the western boundary currents

Junlu Li, Jianping Gan^{*}

Center for Ocean Research in Hong Kong and Macau, Department of Ocean Science and Mathematics, The Hong Kong University of Science and Technology, Hong Kong, China

Earth, Ocean and Atmospheric Sciences, The Hong Kong University of Science and Technology (Guangzhou), Guangzhou, China

ABSTRACT

The North Equatorial Current (NEC) and western boundary currents (WBCs) of the Kuroshio Current (KC) and the Mindanao Current (MC) characterize the circulation pattern and water mass transports in the tropical western North Pacific. We utilized the validated three-dimensional and time-dependent China Sea Multi-scale Ocean Modeling System to investigate the variability of the WBCs and the physical processes linked with the upstream NEC and associated with the circulation. The latitude-dependent KC and MC strengthen downstream from the NEC bifurcation (NB) and are maintained by the northern and southern parts of the NEC, respectively. By effectively isolating the NEC spatiotemporal modes representing its intensity, meridional migration, and bifurcation location, we investigate the responses of the WBCs to the characteristics in an integrated NEC-WBCs current system. The NEC intensity peaks in spring and summer, while its bifurcation location strongly correlates with its migration. The southward (northward) NEC migration during early spring (late autumn) feeds more NEC waters to the MC (KC). Yet, the simultaneous southward (northward) shifting NB distributes more NEC waters to the KC (MC) and offset the contribution of the migration. Thus, the intensity of the KC (MC) is primarily controlled by the NEC intensity, reaching the maximum during spring (summer). The specific water masses such as the North Pacific Tropical Water and the Equatorial Surface Water, are bounded by the time-dependent NB, distributing northward and southward respectively through the WBCs. By resolving spatiotemporal modes in NEC-KC-MC, the study provides a new understanding to the WBCs in the NEC-WBCs current system.

1. Introduction

The northward flowing Kuroshio Current (KC) and southward flowing Mindanao Current (MC) are situated at the western boundary of the tropical Western Pacific Ocean (WPO). These two western boundary currents (WBCs) are important to the meridional water, heat, and energy transports of the entire WPO. The KC intrudes into the South China Sea (SCS) through the Luzon Strait (LS) (Centurioni et al., 2004; Farris and Wimbush, 1996; Tian et al., 2006) and exchanges physical and biogeochemical substances with the East China Sea (Chen et al., 1995; Liu and Gan, 2012). In contrast to the KC, the MC flows southward and bends eastward at $\sim 5^{\circ}\text{N}$ to join the North Equatorial Countercurrent (NECC), closing the North Pacific tropical gyre. A branch of the MC contributes to the global overturning circulation as part of the Indonesian Throughflow (Gordon, 1986). The MC enters equatorial region with subtropical water in the Pacific warm pool, which significantly affects the heat and freshwater budgets of the equatorial and tropical regions and has impact on the El Niño-Southern Oscillation (ENSO) (Gu and Philander, 1997).

The two WBCs originate from the North Equatorial Current (NEC), whose axis locates around 13°N in the western Pacific and forced by the

prevailing easterly trade winds (Fig. 1) (Nitani, 1972; Qiu and Lukas, 1996; Qu et al., 1998; Toole et al., 1990, 1988). Thus, all three currents are inter-connected to form the NEC-KC-MC (NKM) circulation system. The NEC bifurcates into the WBCs (Fig. 1). The spatiotemporal variability of this current system is crucial to the downstream of the WBCs and further affects the regional ocean circulation and the climate (Gan et al., 2016a; Hu et al., 2015; Nan et al., 2015).

The KC and MC are two typical WBCs which are strong, narrow and thick. They have widths of ~ 200 km and depths of ~ 500 m. Although previous studies were based on different models, datasets or different time periods, they all generally found that the maximum velocities of these two currents exceed 0.8 m s^{-1} (Hu et al., 2015; Kashino et al., 2009, 2005; Qu et al., 1998; Ren et al., 2018). For the mean state, early studies using hydrographic data and reduced-gravity models revealed that the KC is stronger than the MC (Nitani, 1972; Qiu and Lukas, 1996; Toole et al., 1988). More recently, studies utilizing *in situ* current measurements, Argo floats, and realistic circulation models revealed that the MC was the stronger current (Gan et al., 2016b; Kashino et al., 2009; Qu et al., 1998; Wang et al., 2015). In addition, the seasonal variations of the KC and the MC are reported to be in-phase in some studies (Gan et al., 2016b; Tozuka et al., 2002), but out-of-phase in other studies (Kim

^{*} Corresponding author.

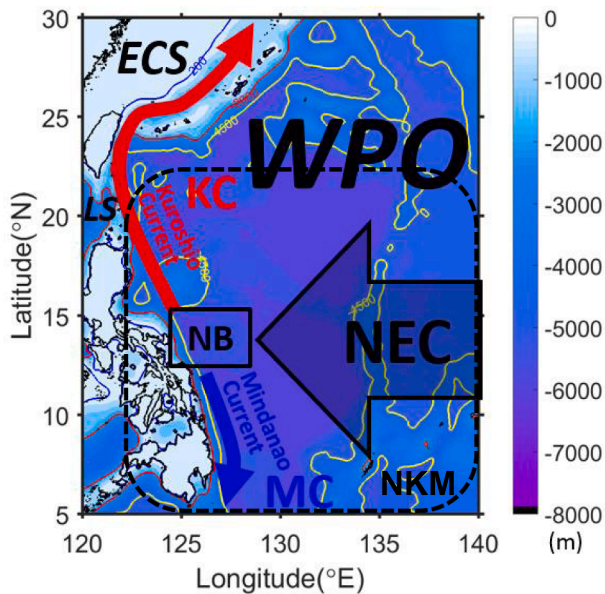


Fig. 1. Bathymetry (m) and schematic of the upper layer circulation in the Western Pacific Ocean (WPO). The WPO connects to marginal seas such as the South China Sea (SCS) through Luzon Strait (LS) and to the East China Sea (ECS) via the continental slope. The North Equatorial Current (NEC), Kuroshio (KC), and Mindanao Current (MC) link at the NEC Bifurcation (NB). The NEC-KC-MC (NKM) circulation region is indicated by the dashed box.

et al., 2004; Qiu and Lukas, 1996). The discrepancies remained in the previous studies may be caused by their different observational periods or physical setting of the simulations. The lack of observational data generates ambiguous understanding of the NKM circulation. Apparently, characteristics of the spatiotemporal variability, processes, and underlying physics are crucial to determine variability of the NKM circulation system and clarify the existing ambiguity.

The upstream NEC controls the KC and MC, while the local dynamics at the western boundary modulate the WBCs. As a result, the structure, intensity, and variability of the NEC affect how the KC and the MC respond to different physical processes in the NEC. The basin-scale wind-driven NEC ranges from $\sim 6^\circ\text{N}$ to $\sim 20^\circ\text{N}$, and the NEC deepens northward (Nitani, 1972; Qiu and Lukas, 1996; Qu et al., 1998; Toole et al., 1990; Toole et al., 1988). The southward-intensified structure and the variability of the NEC (Kim et al., 2004; Qiu et al., 2013; Zhai et al., 2013; Zhang et al., 2017) affect how the NEC water is distributed into the KC and the MC but have not been adequately investigated. In addition to the basin-scale NEC characteristics, the NEC bifurcation (NB) that links the NKM circulation also determines the nature of the NEC partition. NB divides the NEC into northern (NEC_N) and southern (NEC_S) streams that directly feed into the KC and MC, respectively. As a result, the meridional migration of NB affects the intensities of the KC and MC.

Based on the significant seasonality in the NKM circulation system (i. e., the NEC, KC, MC, and NB), we focus on the inter-connection of the currents and NB in seasonal time-scale in this study. The seasonality and transport of the NEC were reported to be variable with longitude across the North Pacific basin (Liu and Zhou, 2020). Specifically, in the focused region of the western North Pacific, the annual mean transport of the NEC is $\sim 50\text{ Sv}$, and the current varies seasonally, peaking in spring and summer (Qu et al., 1998; Liu and Zhou, 2020). The seasonally varying transport and the time-dependent meridional structure of the current characterize the westward flowing NEC, and jointly determine the characteristics of the KC and the MC after the NEC bifurcates east of the Philippines coast. Due to the variation of wind stress curl (WSC), the NB is in the south from spring to summer and in the north during late autumn (Qu and Lukas, 2003). Some previous studies have revealed the

seasonality of the independent NEC, KC, MC, and NB. However, there are few studies that investigate the direct connection between the NEC/NB and the WBCs intensities in seasonal timescale. Kim et al. (2004) utilized a high-resolution model to cross-correlate between the NKM currents and the NB in inter-annual timescale. The statistical analysis of their study showed the existence of general correlations between the NB and the WBCs, but the seasonal correlation and underlying physics for the inter-connections within the NKM system were not investigated. Moreover, a method to quantify the contributions of the NEC/NB to the WBCs, under the linked physical processes, does not exist.

In this study, we utilized a physically and observationally validated three-dimensional ocean circulation model to conduct physics-oriented analyses of the WBCs and the associated NKM current system in the WPO. We identify the spatiotemporal characteristics and variability of the NEC, WBCs, NB, and their physical inter-connections in the seasonal timescale. Based on a novel diagnostic approach, we quantify the contributions of NEC to the WBCs under different physical processes such as the intensity (INT) and meridional migration (MIG) of the NEC and the variation of NB (BIF). Finally based on the qualitative and quantitative study, we investigate the time- and depth-dependent NB and its related water mass distribution in the western North Pacific.

2. Description of the ocean model

We used the China Sea Multiple-scale Ocean Modeling System (CMOMS) (Gan et al., 2016a, 2016b), which is based on the Regional Ocean Model System (ROMS) (Shchepetkin and McWilliams, 2005), to conduct a dynamical study of the WBCs and the circulation in the WPO. We adopted a local closure scheme in the vertical mixing parameterization that is based on the level-2.5 turbulent kinetic energy equations by Mellor and Yamada (1982). The model domain extends from $\sim 0.95^\circ\text{N}$, 99°E in the southwest corner to $\sim 48.5^\circ\text{N}$, 143°E in the northeast corner, and contains all the China Seas, the Japan Sea, and part of the WPO. For the coastline and water depth, we merged ETOPO5 data from the National Geophysical Data Center with digitized water depths extracted from the navigation maps published by the China Maritime Safety Administration. The horizontal resolution of the model is $\sim 10\text{ km}$ in the southern part and gradually increases to $\sim 7\text{ km}$ in the northern part. Vertically, we adopted 30-layer stretched terrain-following coordinates, which have higher resolution in the pycnocline depth and surface/bottom boundary layers.

The model is forced with the wind stress derived from the daily blended 0.25° -degree sea surface winds released by National Oceanic and Atmospheric Administration (NOAA) and the National Climatic Data Center (NCDC, <http://www.ncdc.noaa.gov/oa/rsad/blendedseawinds.html>), based on the bulk formulation (Fairall et al., 2003). We calculated the heat and salt flux forcing from daily reanalysis meteorological data released by the National Centers for Environmental Prediction (NCEP) using bulk formula. We applied active open boundary conditions (OBCs), which integrated the active OBCs (Gan and Allen, 2005) and Tidal-Subtidal (TST) OBCs (Liu and Gan, 2016), to concurrently accommodate tidal and subtidal forcing along the eastern and southern open boundaries of the model domain. At the western boundary and most of the northern boundary, we applied closed boundary condition since they reached the land of southeast Asia. The three-dimensional subtidal velocities, temperature, salinity and two-dimensional sea surface height along the open boundaries were derived from the Ocean General Circulation Model for the Earth Simulator (OFES) global model (Sasaki et al., 2008). The tidal forcing, with eight harmonic constituents (M_2 , S_2 , N_2 , K_2 , K_1 , O_1 , P_1 , and Q_1), was derived from the Inverse Tide Model (ITM) (Egbert et al., 1994).

The model was spun up with climatological monthly atmospheric forcing and lateral fluxes for 50 years. The model was then initialized by the winter-mean results averaged in the last 5 years of the climatological case to conduct direct simulation with daily atmospheric forcing (adopted from NOAA and NCEP) and lateral fluxes (adopted from OFES)

from 1988 to 2012. The model results from 1993 to 2012 were used for our analyses. The detailed configuration and validations of the model can be found in previous studies (Gan et al., 2016a,2016b; Liu and Gan, 2017).

3. Characteristics of the NKM circulation in the WPO

3.1. Mean three-dimensional circulation

The annual mean northeasterly wind dominates the NKM region (Fig. 2a). The zero-line at $\sim 15^\circ\text{N}$ divides the WSC over the NKM region. Negative and positive WSC dominate the northern and southern halves of the NKM region, respectively. The WSC in the subtropical region fluctuates seasonally with alternating negative and positive values over the year, and the intensities of the wind stress (not shown) and WSC peak in winter (Fig. 2b). The zero WSC line migrates southward in spring and northward in autumn. The WSC largely determines the location of the basin-scale NEC, based on the Sverdrup balance.

The wind-driven basin-scale NEC extends from $\sim 6^\circ\text{N}$ to a latitude north of 18°N meridionally and has a southward-intensified structure.

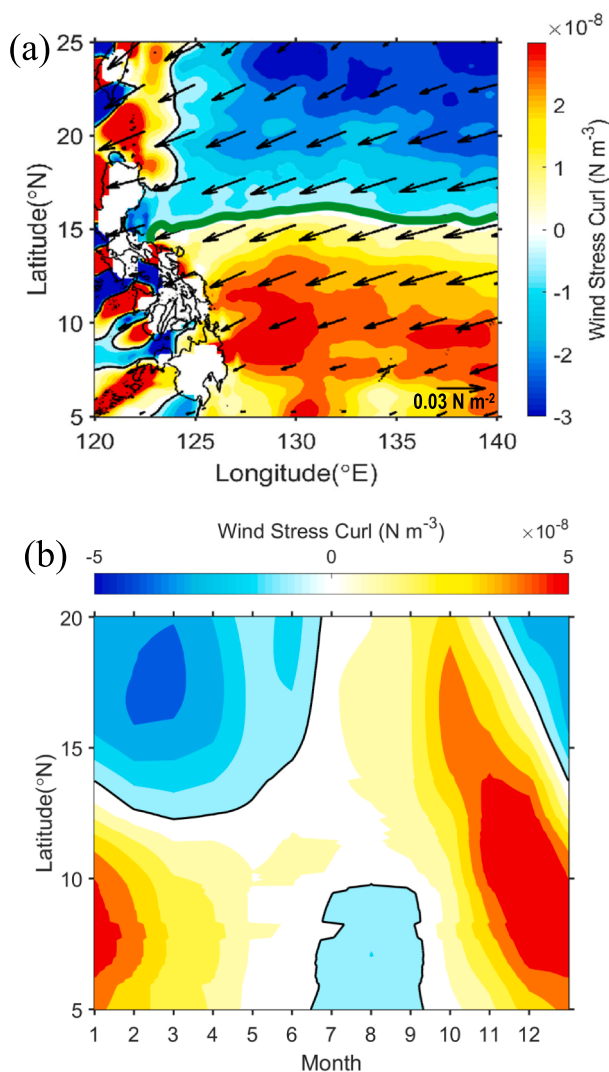


Fig. 2. (a) Annual mean wind stress (N m^{-2} , vectors) and wind stress curl (N m^{-3} , color-shaded) over the NKM region and (b) seasonal variability of the zonally-averaged wind stress curl within the NKM region (dashed box in Fig. 1). The green line in (a) denotes the zero wind stress curl in the focused NKM region. The black line in (b) denotes the zero contour of the zonally-averaged wind stress curl.

Because of the wind forcing, the circulation in the WPO exhibits unique spatiotemporal characteristics. We adopted the satellite altimetry data including the surface absolute geostrophic velocity and sea surface height anomaly to validate our model results. The satellite data is processed by the Data Unification and Altimeter Combination System (DUACS) and provided by the Copernicus Marine Environment Monitoring Service (CMEMS). The depth-averaged velocity in the upper 100 m and the surface velocity adopted from satellite data all exhibit a maximum velocity of $>0.2 \text{ m s}^{-1}$ at $\sim 10^\circ\text{N}$ (Fig. 3a and b). Off the east coast of the Philippines, the NEC bifurcates into the two intensified WBCs. The northern branch (KC) brings the NEC water northward. The southern branch (MC) feeds into the Celebes Sea and the tropical/equatorial region. The KC and MC are strong and narrow with widths of $\sim 250 \text{ km}$. According to the spatial patterns of the NKM circulation and the WBCs, we defined the NKM and WBC domains as the black and the red boxes in Fig. 3b, respectively. The NKM domain is surrounded by sections bounded by 8°N , 130°E , 18°N . The WBC domain encompassed the KC and MC in the meridional area bounded by 8°N to 18°N and from the coast to $\sim 250 \text{ km}$ offshore. The eastern boundary of the WBC domain is generally parallel to the coastline of the Philippines.

The sea surface height anomaly (SSHA) reflects the pattern of surface circulation (Fig. 3c, d). The gradient of the SSHA represents the intensities of the upper layer currents based on the dominant geostrophic balance in the upper layer of the ocean. The SSHA in the WPO generally increases poleward (Fig. 3c, d). In Fig. 3, a prominent low SSHA is found at $\sim 6^\circ\text{N}$ east of the Mindanao Island that is caused by positive WSC induced cyclonic tropical gyre (i.e. NEC, MC, and NECC). The significant zonal gradients of SSHA situate along the Philippines coast corresponding to the WBCs, which are caused by the western intensification. In addition, relatively strong meridional gradients of the SSHA are found in the maximum velocity centers of the southward-intensified NEC and in the eastward NECC.

Vertically, the cores of the NEC, KC, and MC are mainly trapped in the upper $\sim 500 \text{ m}$ (Fig. 4). The NEC extends northward to $\sim 20^\circ\text{N}$, and thickens due to the northward deepening of the pycnocline caused by the wind-induced subtropical gyre (Fig. 4a), which was reported by previous observational studies (e.g. Qiu et al., 2013; Toole et al., 1990; Wang et al., 2015). The maximum velocity core of the NEC is $>0.2 \text{ m s}^{-1}$ and situates on the southern side. The strong eastward NECC at $\sim 6^\circ\text{N}$ borders with the southern boundary of the westward NEC. The eastward jets below the NEC are the North Equatorial Undercurrent (NEUC) jets (Li and Gan, 2020; Qiu et al., 2013). The southernmost NEUC jet is the strongest with a maximum velocity of $>0.05 \text{ m s}^{-1}$ and the northern two jets are weaker, which has also been revealed by the World Ocean Atlas (WOA) and Argo profiler data (Qiu et al., 2013; Wang et al., 2015).

The velocity cores of the KC and the MC are trapped within $\sim 250 \text{ km}$ of the western boundary layer with strong vertical and horizontal shears (Fig. 4b, c). Below the northward KC, the southward Luzon undercurrent (LUC) has a core velocity of $>0.03 \text{ m s}^{-1}$ and extends below 1500 m. Similarly, the northward Mindanao Undercurrent (MUC) has a core velocity of $>0.05 \text{ m s}^{-1}$ and exists under the MC. The structures and intensities of the mean surface and sub-surface currents across 130°E , 18°N and 8°N sections (Fig. 4) from our simulation are well consistent with the previous observational studies (Hu and Cui, 1989; Hu et al., 1991,2013; Qiu et al., 2013; Wang et al., 2015).

According to the vertical structure of the depth-dependent NKM circulation, the upper NKM layer and the undercurrent layer below are separated by the isopycnal surface with a potential density of $\sigma_\theta = 26.8 \text{ kg m}^{-3}$ (Fig. 4). The existence of a weaker undercurrent system and the spatial characteristics of the NEUC jets, the LUC, and the MUC were observed in many studies (Hu et al., 2013; Qiu et al., 2013; Ren et al., 2018; Schönau and Rudnick, 2015; Zhang et al., 2014; Zhang et al., 2017). The NKM and the undercurrents couple vertically, reflecting the complex baroclinicity and nonlinearity of the interlinking currents in the three-dimensional circulation of the WPO. The characteristics of the NKM and the undercurrent system reported in previous studies (e.g. Qiu

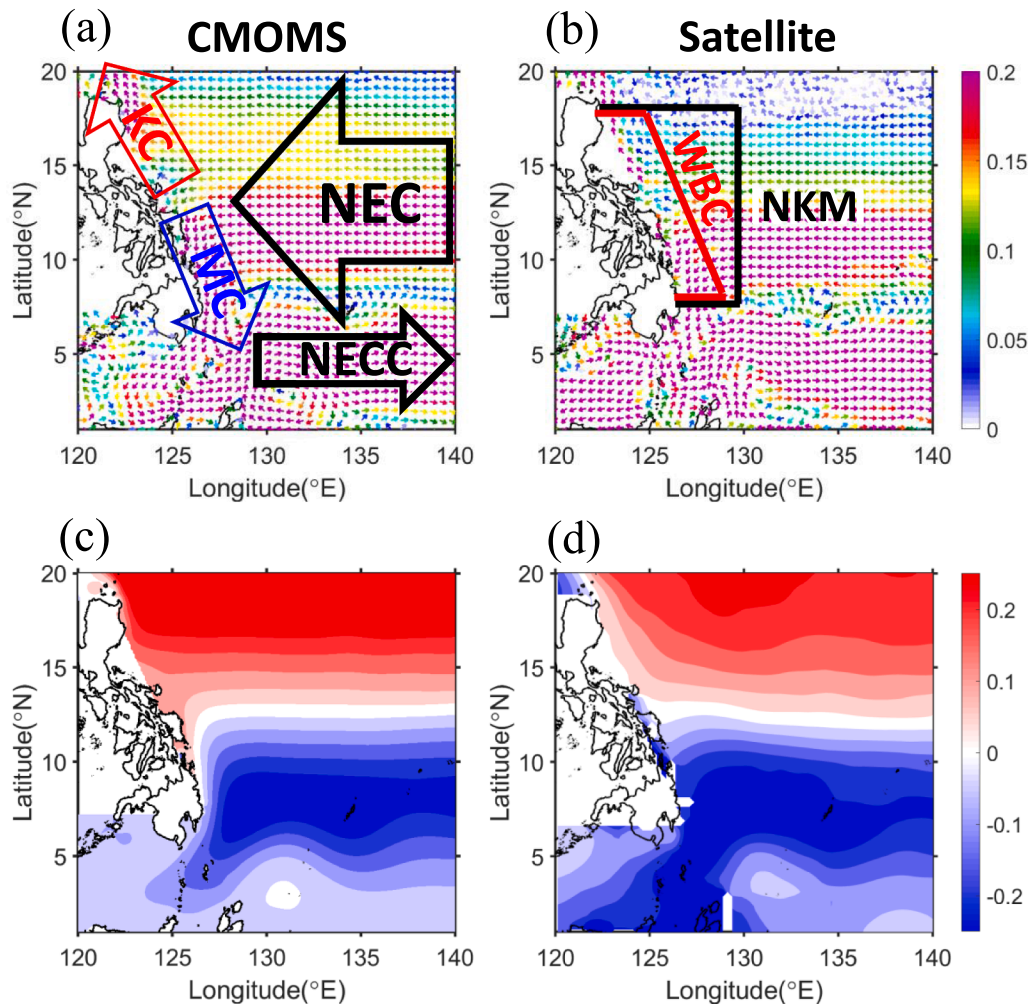


Fig. 3. The annual mean (a) horizontal velocity (m s^{-1}) averaged within 0–100 m adopted from the model simulation and (b) surface velocity (m s^{-1}) adopted from satellite data. The annual mean sea surface height anomaly (m) adopted from the (c) model simulation and (d) satellite data. The data is averaged from 1993 to 2012. The black and red boxes between 8° and 18°N in (b) define the domain of the NKM and the WBC, respectively.

et al., 2013) are qualitatively and quantitatively captured by our model shown in Fig. 4.

The intensity and structure of the WBCs are latitude-dependent. The northward KC and the southward MC gradually strengthen downstream from the location of NB (Fig. 5a). The velocity cores of the KC and the MC attach closely to the Philippine coast at all latitudes. The KC has a maximum velocity of $>0.6 \text{ m s}^{-1}$ at the east of Luzon Island, and weakens southward, and the southward MC becomes significant south of 13°N and reaches a maximum velocity of $>0.8 \text{ m s}^{-1}$ at 9°N .

NB is the origin of the WBCs and is where the NEC bifurcates, and serves as the connecting point of the WBCs and the NEC. Thus, NB is defined as the location where the meridional velocity, zonally averaged within the NKM domain (black box in Fig. 3b), is zero (Fig. 5b). The annual mean NB in the NKM layer locates at 14.9°N . In the upper $\sim 50 \text{ m}$, because of the northward Ekman transport induced by the easterly trade winds, NB locates significantly south near the surface. The NB shifts to a higher latitude with the increase of depth gradually due to the northward thickening of the NEC, and reaches 16°N at the bottom of the NKM layer (Fig. 5b). This NB northward shift with depth was reported in many previous studies that utilized historical hydrographic data and model simulations (Jensen, 2011; Kim et al., 2004; Qu and Lukas, 2003; Qu et al., 1998; Yaremchuk and Qu, 2004).

The NEC waters can be divided from the mean NB location into northern and southern branches. The northern branch (NEC_N) is the westward transport integrated from the mean NB location at 14.9°N to

18°N and the southern branch (NEC_S) covers from 8°N to 14.9°N . The NEC_N and NEC_S directly feed into the northward KC and southward MC, respectively. The coherent links among different components of the currents in the NKM are reflected in the corresponding linkage of their respective water masses (Fig. 6). Similar vertical density profiles between the NEC_N and the KC, and between the NEC_S and the MC (Fig. 6a) evidence their connectivity, respectively. We have also proved the relation between the KC (MC) and the NEC_N (NEC_S) by the Lagrangian trajectory of the water parcels. The NEC mainly carries three types of water masses: North Pacific Tropical Water (NPTW), North Pacific Intermediate Water (NPIW), and a mixture of NPIW and Antarctic Intermediate Water (AAIW). The subsurface NPTW with high temperature and high salinity is mainly trapped north of $\sim 12^\circ\text{N}$, while the NPIW is below the NPTW with minimum salinity (Qu et al., 1998, 1999). Main portions of the NPTW and the NPIW are constrained in the NEC_N and flow directly into the KC, while the MC extracts the NEC_S water, which mainly consists of the mixed NPIW and AAIW (Fig. 6b). The T-S water mass properties in the currents are also consistently shown from the Generalized Digital Environment Model (GDEM) (Carnes, 2002) in Fig. 6b.

3.2. The link between the WBCs and the NEC

Unlike the earlier studies that link the WBCs with individual NEC or NB, we found that intensity, meridional migration, and the location of

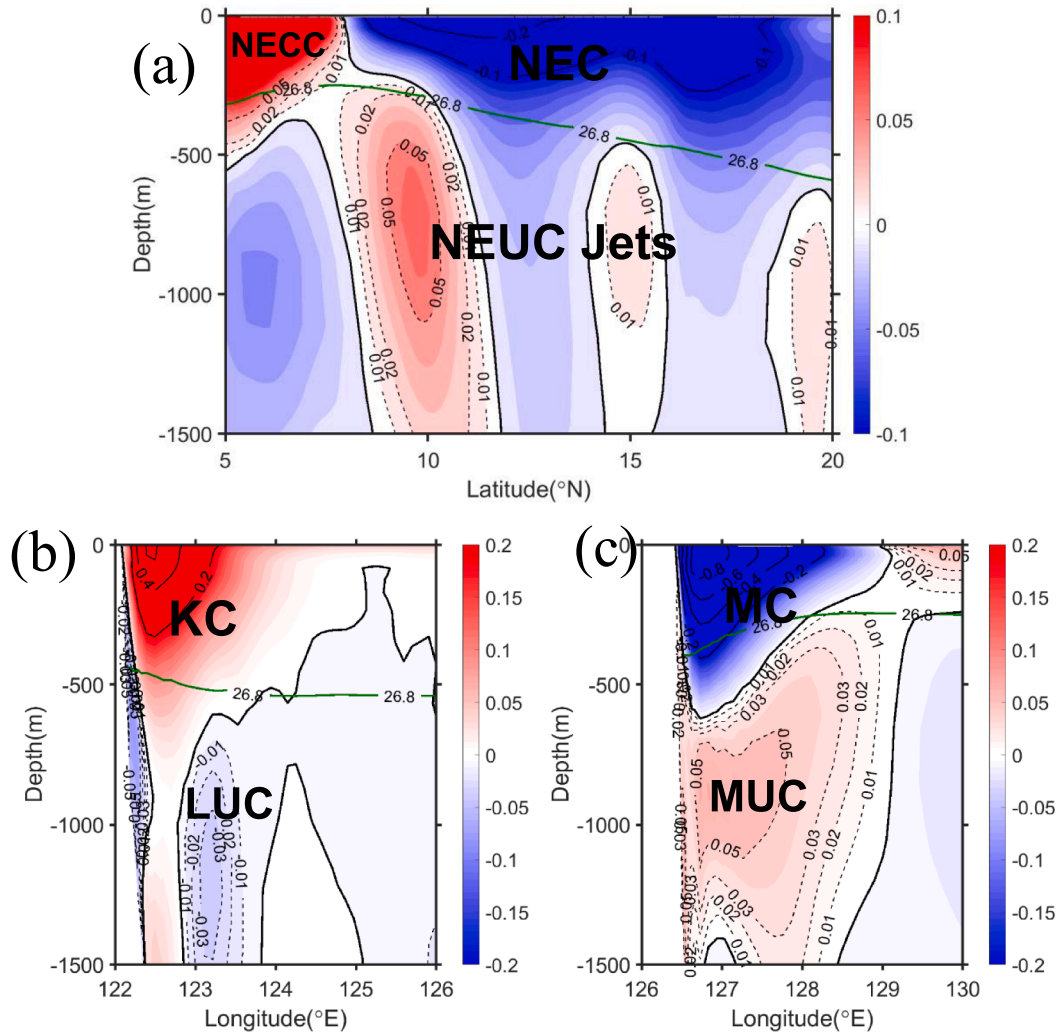


Fig. 4. Cross-section of velocity (m s^{-1}) along (a) 130°E , (b) 18°N , and (c) 8°N representing the NEC, KC, and MC, respectively. Positive values indicate eastward flow in (a) and northward flow in (b) and (c). The North Equatorial Countercurrent (NECC), North Equatorial Undercurrent (NEUC) Jets, Luzon Undercurrent (LUC) and Mindanao Undercurrent (MUC) are shown in the figures. The green line denotes the isopycnal surface of potential density equal to 26.8 kg m^{-3} . The data is adopted from the model simulation.

NB control the WBCs, and these three processes interact with each other to jointly govern the variability of the WBCs. This section details how each of the processes affect the WBCs.

3.2.1. NEC intensity

Forced by the easterly trade wind, the intensity of the NEC is seasonally variable. The annual mean NEC transport, integrated from 8°N to 18°N along the 130°E section, is $\sim 40 \text{ Sv}$ (Fig. 7). The transport of the KC at 18°N is $\sim 14 \text{ Sv}$, which is smaller than the MC transport of $\sim 26 \text{ Sv}$ at 8°N (Fig. 7). The transports of KC and MC are integrated from the coast to 130°E , which are consistent with transports integrated within the real widths of the WBCs, that is, $\sim 200 \text{ km}$ off-shore. The transports of all three currents are slightly smaller than the previous observations because the water transports below the physical bottom (isopycnal surface: $\sigma_\theta = 26.8 \text{ kg m}^{-3}$) of the NKM layer are not included (Fig. 4). However, the seasonal variation and major features of the currents transports are not affected. Based on Sverdrup's theory, the NEC is strong in spring to summer and weak in late autumn due to the seasonal variability of the wind forcing (Sverdrup, 1947). The intensity of the NEC largely determines the intensities of the KC and MC. The KC transport has a similar seasonality as the NEC transport peaking in spring and summer, while the MC transport peaks in summer. All three

currents are weak in autumn to winter. The features and seasonal variations of the NEC and the WBCs are generally consistent with previous historical observations and numerical simulations (Qiu and Lukas, 1996; Qu et al., 2012, 1998; Yaremchuk and Qu, 2004).

We divided the volume flux of the NEC into latitude-independent (\bar{U}) and latitude-dependent portions (U')

$$U = \bar{U} + U' \quad (1)$$

where \bar{U} is the mean of the depth-integrated (above the isopycnal surface: $\sigma_\theta = 26.8 \text{ kg m}^{-3}$) westward volume flux averaged from 8° - 18°N along 130°E . U' is the corresponding spatial anomaly. The physical meaning of the \bar{U} and U' for the annual mean NEC profile is presented in Fig. 8a. To depict spatial variation of the NEC, we separate NEC by referencing to its annual mean NB location of 14.9°N , such that \bar{U} integrated from 14.9° to 18°N and from 8° to 14.9°N represent mean north and south NEC transports, respectively.

3.2.2. NEC migration

As shown in Fig. 3, the NEC meridional structure intensifies southward. The annual mean volume flux of the NEC, as a function of latitude, is shown in Fig. 8a. The large standard deviation (STD), shaded area in

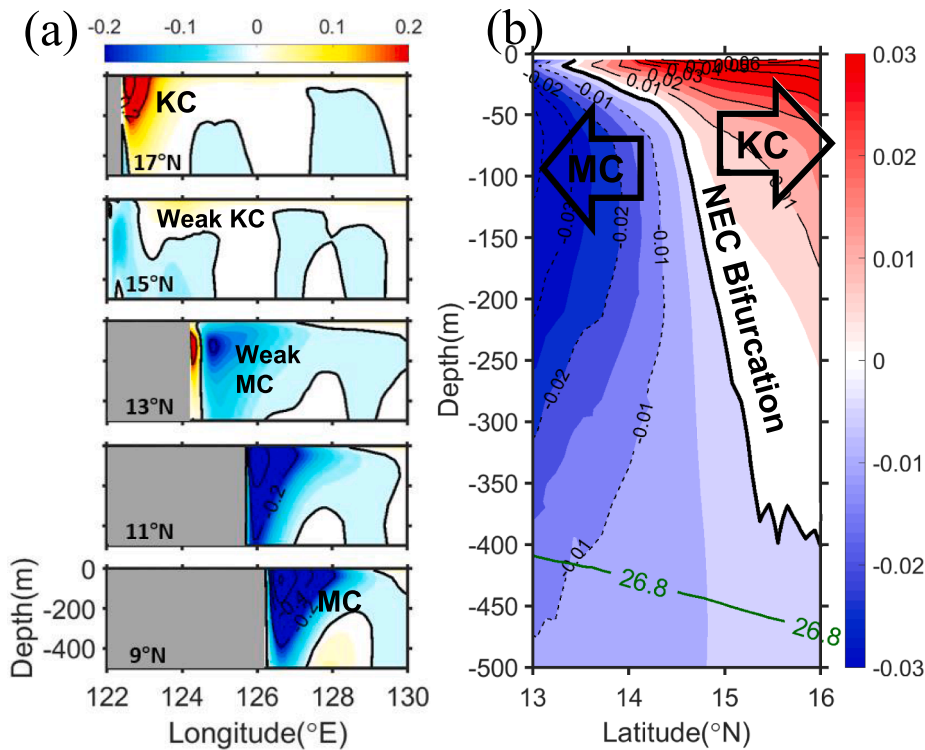


Fig. 5. (a) Meridional velocity (m s^{-1} , positive values refer to a northward current) along different latitudinal sections off the Philippine coast; (b) zonally averaged meridional velocity (m s^{-1}) within the NKM domain (black box in Fig. 3b, i.e. from the coast to 130°E) as a function of depth and latitude. Thick solid line denotes the zero contour of the velocity.

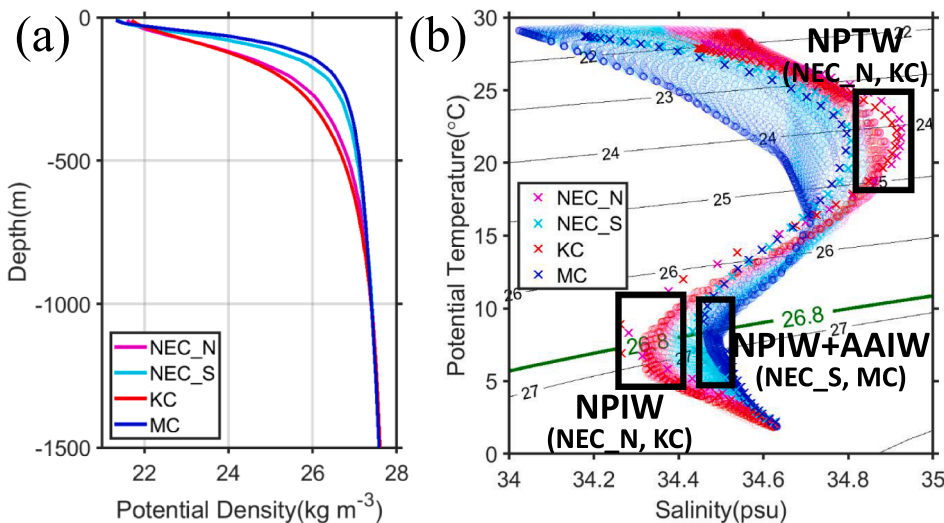


Fig. 6. (a) The potential density averaged in NEC_N and NEC_S along 130°E , the KC along 18°N from the east coast of the Philippines to 130°E , and MC along 8°N from the east coast of the Philippines to 130°E . (b) The T-S diagram at different sections. The distinct North Pacific Tropical Water (NPTW), North Pacific Intermediate Water (NPIW), and Antarctic Intermediate Water (AAIW) masses are indicated by the black boxes. The circles denote the model simulation data, and the crosses denote GDEM data in (b).

Fig. 8a), suggests that the NEC varies strongly with time, and is southward-intensified in spring (green line in Fig. 8b), but the core of the NEC moves northward in autumn (yellow line in Fig. 8b). The time series of the westward volume flux shows that the NEC migrates to the south from February to July and to the north from September to November (Fig. 8c).

Thus, by adopting Eq. (1), we can use U' to represent the KC (MC) transport contributed by the NEC migration effect. When the NEC migrates to the south (north) in spring (autumn), the NEC feeds more water into the MC (KC). As a result, the NEC migration effect (U') becomes a sink (source) for the KC (MC) in early spring and is a source (sink) for the KC (MC) in late autumn (magenta lines in Fig. 8).

3.2.3. NEC bifurcation

The westward transport of the NEC is distributed northward and southward by NB at the western boundary, which forms the downstream intensified KC and MC (Fig. 5a), respectively. Given the annual mean NB locating at 14.9°N , a larger portion of the NEC between 8° and 18°N is distributed to the MC at the annual time-scale (Figs. 7 and 9). Seasonally, the NB shifts to the south in early spring and to the north in late autumn, which is consistent with the previous observations and model simulations (Fig. 9) (Chen and Wu, 2011; Kim et al., 2004; Qu and Lukas, 2003).

Apparently, the variability of NB alters the distribution of NEC, and the spatiotemporal variations of the KC and MC. To better depict the

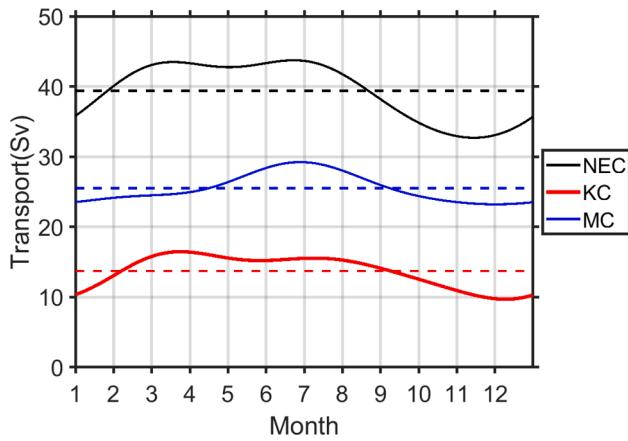


Fig. 7. The seasonal volume transport (Sv) of the NEC (along 130°E, 8° to 18°N), KC (along 18°N, coast to 130°E), and MC (along 8°N, coast to 130°E). Dashed lines denote the annual mean transports.

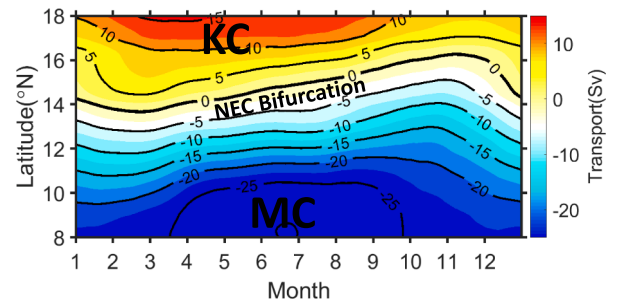


Fig. 9. Seasonal variation of the layer-integrated meridional volume transport (Sv) within the NKM domain (Fig. 3b). Positive and negative values denote the northward KC and southward MC, respectively. The zero-transport contour indicates the location of NEC bifurcation (NB).

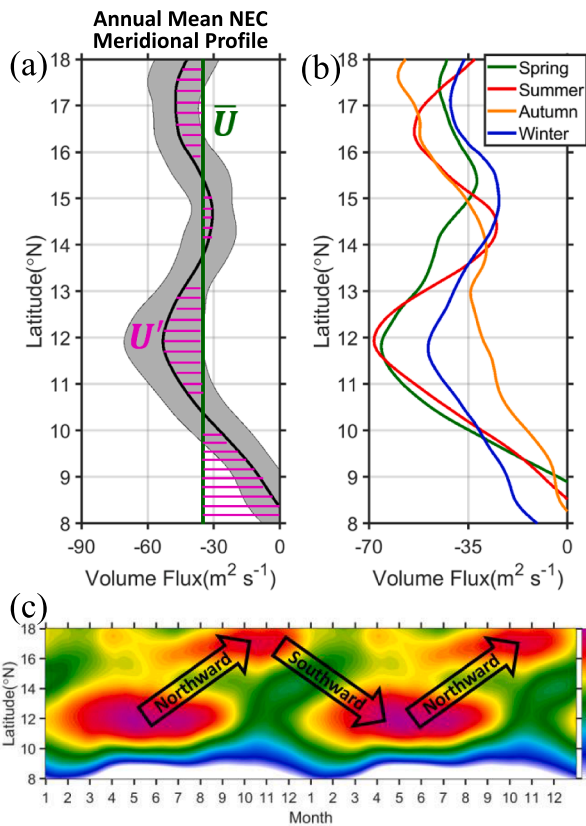


Fig. 8. (a) Meridional variation of the annual mean (solid line) zonal volume flux ($m^2 s^{-1}$) of the NEC and the standard deviation (shaded). \bar{U} and U' in Eq. (1) are indicated in (a). (b) The seasonal mean volume flux ($m^2 s^{-1}$) of the NEC. (c) Zonal volume flux ($m^2 s^{-1}$) integrated over the depth of the NEC layer along 130°E as a function of time and latitude. A repeated two-year cycle is shown.

seasonal variations of the KC and MC that are influenced by NB, the meridional volume transports across annual mean NB of 14.9°N between the Philippine coast and 130°E is used to define the transport that contributes to the KC (northward) or MC (southward). In early spring when NB is in the south, the transport across 14.9°N is northward and more NEC water is distributed to the KC (Fig. 10a). The opposite occurs in late autumn when NB moves north and more NEC waters is distributed to the MC (Fig. 10b).

3.2.4. Inter-connection of the NEC intensity, migration and bifurcation

As mentioned previously, the intensity of the NEC is dynamically controlled by the WSC based on Sverdrups theory. The meridional migration of the NEC is also linked with the wind field, especially determined by the location of zero WSC. The basin-scale atmospheric forcing has a significant seasonality, in terms of the strength and the latitudinal location (Qiu and Lukas, 1996). Thus, the intensity and migration of the NEC respond to the time-dependent wind field, exhibiting strong correlation in the seasonal time-scale. In addition, the local monsoon with significant seasonality modulates the surface NB location through Ekman dynamics.

The seasonal variability of the upper layer-averaged NB is highly correlated with the variability in the NEC meridional migration (Fig. 8c), this is, when the NEC is in the south during early spring, NB also stays in the south, and in late autumn they are both in the north. The southward (northward) NEC migration during early spring (late autumn) tends to feed more waters to the MC (KC). Yet, the simultaneous southward (northward) shifting NB distributes a larger portion of the NEC water to the KC (MC) and offset the contribution of the migration.

The atmospheric field fundamentally controls the NEC intensity and migration via the WSC strength and spatial pattern respectively, and the NEC migration directly determines the location of the NB. Meanwhile, the local wind forcing slightly modulates the NB within the Ekman depth, but not affecting the whole upper layer. Thus in the seasonal time-scale, the NEC intensity, NEC migration and location of the NB exhibit correlated variation.

3.2.5. Role of NEC intensity, migration, and bifurcation on the WBCs

The joint effect of the NEC intensity, the NEC migration, and the NEC bifurcation on WBCs is complex and overlapped in time and space domains. We construct a diagnostic system to quantify the contributions of the NEC intensity (INT), migration (MIG) and bifurcation (BIF) to the WBCs transports. The volume conservation of these three components, or called IMB (INT, MIG and BIF), is separated into different spatial and temporal modes representing specific physical meanings to identify their inter-linked variability.

By considering IMB volume transports across the boundaries of the NKM domain shown in Fig. 3b, the transports of the KC and the MC can be attributed to mean NEC intensity averaged along 130°E (i.e. INT, $\bar{U}_{8^\circ N-18^\circ N}$), its spatial anomaly (i.e. MIG, $U'_{8^\circ N-18^\circ N}$) and northward velocity due to bifurcation (i.e. BIF, $\int_{coast}^{130^\circ E} V dx$) in the northern domain (14.9°N-18°N) and southern domain (8°N-14.9°N), respectively:

$$KC \text{ Transport} = \underbrace{\int_{14.9^\circ N}^{18^\circ N} (\bar{U}_{8^\circ N-18^\circ N}) dy}_{INT} + \underbrace{\int_{14.9^\circ N}^{18^\circ N} (U'_{8^\circ N-18^\circ N}) dy}_{MIG} + \underbrace{\int_{coast}^{130^\circ E} V dx}_{BIF} \quad (2)$$

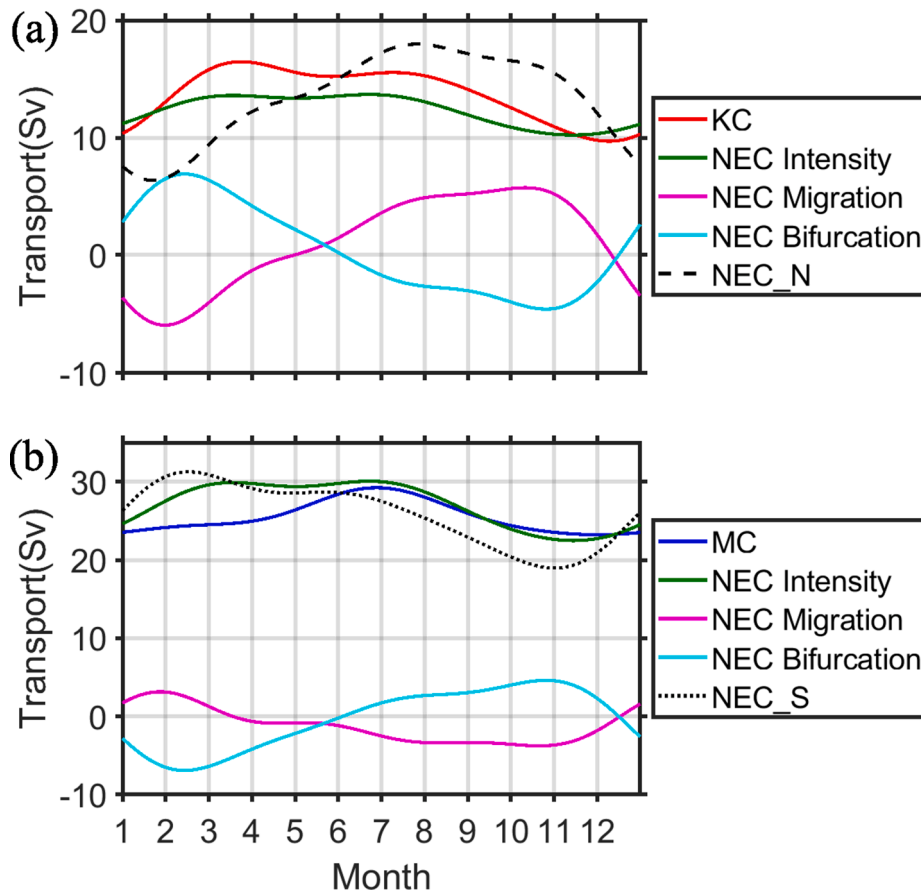


Fig. 10. Seasonal volume transport (Sv) of (a) the KC and (b) the MC, and the controlling NEC intensity (INT), NEC migration (MIG), and NEC bifurcation (BIF). NEC_N and NEC_S represents the transport of NEC integrated from 14.9°N to 18°N and to 8°N, respectively.

$$MC\ Transport = \underbrace{\int_{8^{\circ}N}^{14.9^{\circ}N} (\overline{U_{8\sim 18^{\circ}N}}) dy}_{INT} + \underbrace{\int_{8^{\circ}N}^{14.9^{\circ}N} (U'_{8\sim 18^{\circ}N}) dy}_{MIG} + \underbrace{\int_{coast}^{130^{\circ}E} V dx}_{BIF} \quad (3)$$

where $\overline{U_{8\sim 18^{\circ}N}}$ is longitudinally (from 8° to 18°N along 130°E) averaged and layer-integrated westward (positive) volume flux above the isopycnal surface: $\sigma_{\theta} = 26.8\text{ kg m}^{-3}$ in the NKM domain. As a result, the integration of $\overline{U_{8\sim 18^{\circ}N}}$ (first terms on the right-hand side of Eqs. (2) and (3)) represents the INT contribution to the transports of the WBCs. The integration of $U'_{8\sim 18^{\circ}N}$ from 8° to 18°N is zero according to its definition, and the second terms of Eqs. (2) and (3) with different integration area represents the transports arising from the effect of NEC south-north migration (MIG) on the KC and MC transport, respectively. V is the layer-integrated northward (positive) volume flux at 14.9°N where the annual mean NB is located. The third terms of Eqs. (2) and (3) represent BIF, which are opposite and indicate the transport across the mean NB section caused by meridional shift of the bifurcation. To identify the contribution from variations of the NEC bifurcation and migration to the WBCs, we use mean NB of 14.9°N as reference location to separate the northern and southern domain in order to effectively isolate the physical processes embedded in the NEC that is contributing to the KC/MC transport. The contributions to KC and MC from the INT vary with the seasonal phases of the NEC transport (Fig. 7). The INT component is strong in spring to summer and weak in late autumn (green lines in Fig. 10). The contribution of the INT to the KC (Fig. 10a) is less than that to the MC (Fig. 10b) because the annual mean NB is located relatively north within the NEC and allows a larger portion of the NEC water to feed the MC.

The MIG represents the movement of the westward NEC profile, and

the BIF indicates the movement of the bifurcation point. These two terms are clearly different with respective physical meaning. The NB varies meridionally in phase with the NEC flux profile shown in Figs. 8c and 9, suggesting that the variations of the MIG and BIF components are highly correlated. However, the contribution by MIG (magenta lines in Fig. 10) to WBCs is opposite to that by BIF (cyan lines in Fig. 10). For example, the southernmost NB during early spring allocates a larger portion of the NEC transport to the KC (i.e., positive BIF for KC in Fig. 10a and negative BIF for MC in Fig. 10b), but the simultaneous NEC southward migration feeds more NEC water to the MC (i.e., negative MIG for KC in Fig. 10a and positive MIG for MC in Fig. 10b). In contrast, the NEC northward migration and the northernmost NB location also contribute opposing effects to the WBCs in late autumn. By isolating the opposite effects of the MIG and BIF on the WBCs, we provide a better understanding of the connection between the WBCs and the characteristics of the NEC.

The NEC_N and NEC_S represent the remote effects from the upstream NEC (i.e., INT and MIG), while the BIF represents the local effect within the WBC region. The annual cycles of the remote upstream NEC_N and NEC_S dominate the magnitudes of the KC and the MC transports respectively, yet, the local BIF component modulates the seasonal variations of NEC_N and NEC_S and, thus, of the KC and MC, respectively (Fig. 10). Seasonally, the northern part of the NEC widens as the bifurcation moves south of the mean NB at 14.9°N, and the northward transport across 14.9°N increases the KC transport. A similar but contrast condition occurs in the southern part of the NEC and the MC as the NB moves north of 14.9°N.

The seasonal pattern and variability of the connection among each component of the NKM are summarized in Fig. 11, exhibiting two unique spatiotemporal modes in early spring and late autumn.

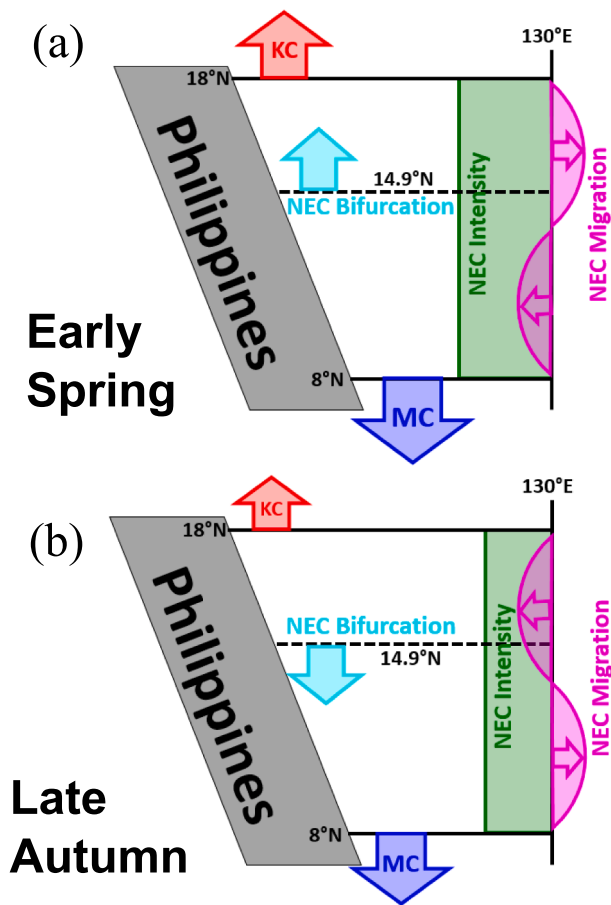


Fig. 11. Schematic of the components that contribute to KC and MC transports: the NEC intensity (INT), NEC migration (MIG), and NEC bifurcation (BIF) in (a) early spring and (b) late autumn. The result shows that the NEC is more intense in spring and less intense in autumn. The southward-intensified NEC and northward-intensified NEC occur in early spring and late autumn, respectively. The relative intensities of KC and MC are represented by the respective size of arrows, and the arrows at the NEC bifurcation represent the transport direction across the annual mean NB location at 14.9°N.

Generally, the contribution of the NEC intensity (INT) dominates the transports of the WBCs at annual and seasonal time scales. Due to the highly correlated but opposing effects of the NEC migration (MIG) and NEC bifurcation (BIF) on the WBCs, the MIG and BIF terms, for the most part, offset each other. In early spring, the NEC is strong with large INT and intensifies southward. The southward migration of the NEC profile contributes positive MIG to the MC transport in the southern part, but negative MIG to the KC transport in the northern part of the NEC (magenta areas in Fig. 11a). In contrast, the southward shifting of the NEC bifurcation provides a northward transport across 14.9°N, and leads to positive and negative BIF contribution of the NEC to the KC and MC respectively (Fig. 11a). In late autumn, the INT component weakens for both WBCs transports, and the effects of the MIG and BIF components on the WBCs are reversed (Fig. 11b).

4. Time- and depth-dependent NB with correlated water mass distribution

The previous studies have revealed that the NB latitude is determined by the basin-scale WSC through the superposition of longitudinal-dependent baroclinic Rossby Wave at the western boundary (Qiu and Lukas, 1996). In consequence, they proved that the NB latitude shifts meridionally by the joint effect of the wind and waves, reaching south in spring and north in autumn. However, as we discussed in the previous

section, the NB variation correlates, and originates from the NEC migration. When the NEC migrates to the north, the water masses contained in the NEC are very likely moves northward simultaneous. As a result, although the NB shifts south and north seasonally, the water mass distribution may not change significantly.

We present the zero line of meridional volume flux integrated from the Philippines coast to 130°E in February and November as the black thick lines in Fig. 12, representing the southernmost and northernmost modes of the NB respectively, to illustrate the time- and depth-dependent NB location. In addition, the salinity averaged in these two months at 130°E are also shown to indicate the characteristics of the water masses, because in the low-latitude region, the salinity is more useful than the temperature to identify different water masses. The contours of the 34.25 psu and 34.85 psu are shown to highlight two important and significant water masses in the NEC: the Equatorial Surface Water (ESW) and North Pacific Tropical Water (NPTW). The ESW has a low salinity due to strong precipitation in the equatorial region and is trapped in the upper tens of meters. At the north of the ESW, the North Pacific Tropical Surface Water (NPTSW) is found with much higher salinity than the ESW. The NPTW ranges vertically from about 100–300 m with a salinity maximum, and is bounded by the South Pacific Sub-surface Water (SPSSW) at the south. More details of the upper layer water mass characteristics can be found in Sun et al. (2008), who provides an overview of the western North Pacific water masses by utilizing Argo data (Sun et al., 2008). In February when the NB locates relatively south in the upper ~500 m, both 34.25 psu and 34.85 psu contours shifts south (Fig. 12a). In contrast, with a northernmost NB, these two significant salinity contours move to the north, and are generally bounded by the depth-dependent NB (Fig. 12b).

To investigate the water masses variation in the WBCs, we present the t-s diagrams of the KC and MC waters in February and November (Fig. 13). The KC (MC) water here is defined as the northward (southward) velocity points at the 18°N (8°N) section from the Philippines

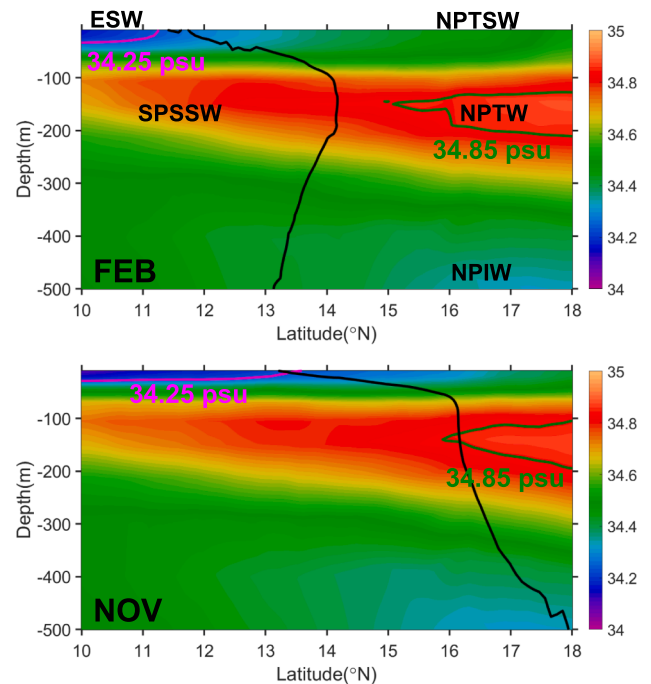


Fig. 12. Salinity at 130°E section in (a) February and (b) November. Magenta lines and green lines denote 34.25 psu and 34.85 psu contours. Black line denotes the zero meridional volume flux integrated from the Philippines coast to 130°E. The Equatorial Surface Water (ESW), North Pacific Tropical Surface Water (NPTSW), North Pacific Tropical Water (NPTW), South Pacific Sub-surface Water (SPSSW) and North Pacific Intermediate Water (NPIW) masses are indicated.

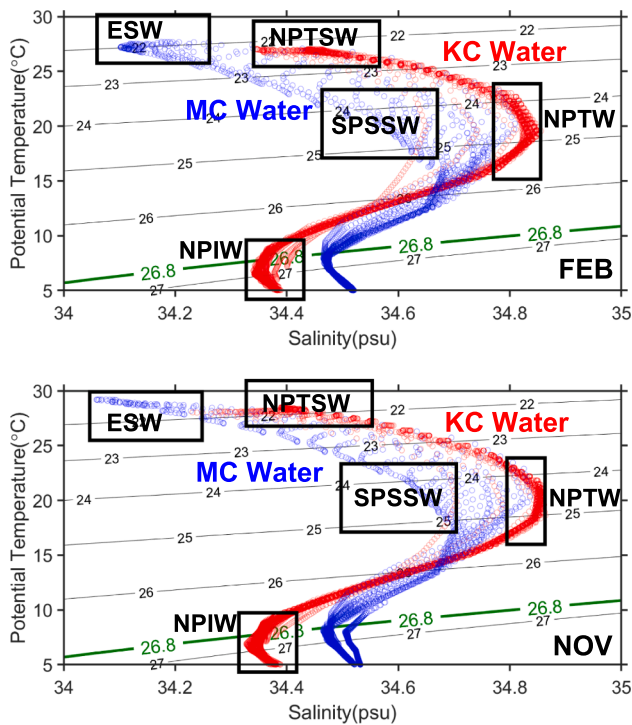


Fig. 13. The t-s diagram of the KC water (red circles, only includes northward velocity points from the Philippines coast to 125°E along 18°N section) and MC water (blue circles, only includes southward velocity points from the Philippines coast to 130°E along 8°N section) in (a) February and (b) November. The Equatorial Surface Water (ESW), North Pacific Tropical Surface Water (NPTSW), North Pacific Tropical Water (NPTW), South Pacific Subsurface Water (SPSSW) and North Pacific Intermediate Water (NPIW) masses are indicated.

coast to 125°E (130°E) in the upper layer. The KC water mainly consists of the surface NPTSW, subsurface NPTW and top of the NPIW, while the MC water mainly consists of the surface ESW and subsurface SPSSW. Apparently, the major compositions of the KC and MC waters have limited change from February to November. The reason has been indicated in Fig. 12 that due to the in-phase meridional migration of the NEC and the NB, the dominant water masses in the NEC distributed into the KC and MC are relatively regular during a year.

The NEC carrying the water masses, i.e. ESW, NPTSW, NPTW and SPSSW, migrates meridionally and correlates with the location in the upper layer. As a result, the temperature and salinity in the northward and southward distributed waters have insignificant changes in a year, due to the simultaneous meridional migration of the whole NEC-NB system.

5. Summary

The NEC, KC and MC are inter-linked in space and time to form and regulate the NKM current system, which is important to ocean circulation and climate variability. Due to the limitation of observations and undefined physical processes in the NKM currents, the detailed spatiotemporal variability of the NEC modes, and the responses of the WBCs as well as the inter-connection within the NKM circulation system, have not been clearly identified. By utilizing a diagnostic method that separate spatial and temporal modes of IMB in the NEC based on principle of volume conservation, we identified processes and physics that connect the NEC, NEC migration, the NB, and the responses in the boundary currents.

Based on a rigorously validated three-dimensional circulation model, we analyze the variabilities of the WBCs in response of the spatiotemporal modes of the NEC, and the consequent NKM circulation pattern

and water distribution in the western North Pacific. We identified the features of the WBCs in response to the spatiotemporal characteristics of the NKM circulation and NEC bifurcation.

The characteristics of the WBCs are closely linked to the NEC, including to its intensity, meridional migration, and location of its bifurcation. The NEC intensity fundamentally determines the total intensity of the WBCs, which is strong during spring to summer and weak during autumn to winter. The NEC migrates northward in late autumn and southward in early spring. Where the NKM currents connect, the variability of NB is directly controlled by the location of the NEC in the upper layer, and modulated by the local wind stress through the Ekman dynamics in the surface. The NEC intensity and meridional migration are basically determined by the atmospheric forcing of the strength and spatiotemporal pattern of the WSC respectively, based on the Sverdrup theory. Thus, the three aspects of the NEC, i.e. intensity, migration and bifurcation, exhibit strong correlation in the seasonal time-scale.

We quantify the contributions of the NEC intensity, NEC migration, and NEC bifurcation to the WBCs by specifying these physical processes with a novel IMB diagnostic method. Based on the method, the KC and MC transports are divided into three components: INT, MIG and BIF, representing the intensity, migration and bifurcation contribution of the NEC to the WBCs, respectively. The MIG and BIF components have significant seasonal variation, but have opposing effects and almost offset each other. Thus, the annual mean transport and seasonal variability of the KC and the MC are both dominated by the INT component and modulated by the MIG and BIF components with strong seasonality. We can clearly identify two representative NEC spatiotemporal modes in early spring and late autumn, with specific INT, MIG and BIF contributions to the WBCs, which has been summarized in Fig. 11.

Based on the quantitative and qualitative study of the NEC spatiotemporal modes of its intensity, migration and bifurcation, we further investigate the water masses distribution in the western North Pacific. In the upper layer, the water masses are generally divided by the time- and depth-dependent NB. The ESW is bounded to the south of the NB while the NPTSW at the north in the upper tens of meters. Below the surface water, the KC and the MC extract NPTW and SPSSW from the NEC respectively. The correlated variation of the NEC migration and NEC bifurcation lead to the insignificant seasonal change of the water properties that distributed northward and southward into the KC and MC, respectively. In this study, we focused on the kinematics of the NKM. During our investigation, we found that the variations of the INT, MIG and BIF modulate the vorticity balance in the NKM region. The balance is dominated by the variation of planetary vorticity associated with the changing transports of the INT, MIG and BIF in the region, while the variation of convergence/divergence of the shear vorticity for the nonlinearity in the WBCs, balances the change of planetary vorticity. A completed analysis of vorticity balance showing the interactive connection among the NEC and the WBCs will be presented in a future study.

Declaration of Competing Interest

The authors declare that they have no known competing financial interests or personal relationships that could have appeared to influence the work reported in this paper.

Acknowledgements

The Key Research Project of the National Science Foundation (41930539) and the Hong Kong Research Grants Council (GRF 16212720) supported our research. CORE is the Center for Ocean Research in Hong Kong and Macau jointly established by QNLM and HKUST. We are also grateful for the support of The National Supercomputing Center of Tianjin and Guangzhou. The CMOMS data used in the paper is produced by Regional Ocean Modeling System (ROMS) and these data can be obtained from <https://odmp.ust.hk/cmoms/>.

References

- Carnes, M., 2002. Data base description for the Generalized Digital Environmental Model (GDEM-V)(U), version 3.0. US Naval Oceanographic Office Tech. Rep 39522-135003.
- Centurioni, L.R., Niiler, P.P., Lee, D.-K., 2004. Observations of inflow of Philippine sea surface water into the South China Sea through the Luzon Strait. *J. Phys. Oceanogr.* 34 (1), 113–121.
- Chen, C., Ruo, R., Paid, S., Liu, C., Wong, G., 1995. Exchange of water masses between the East China Sea and the Kuroshio off northeastern Taiwan. *Cont. Shelf Res.* 15 (1), 19–39.
- Chen, Z., Wu, L., 2011. Dynamics of the seasonal variation of the North Equatorial current bifurcation. *J. Geophys. Res. Oceans* 116 (C2).
- Egbert, G.D., Bennett, A.F., Foreman, M.G., 1994. TOPEX/POSEIDON tides estimated using a global inverse model. *J. Geophys. Res. Oceans* 99 (C12), 24821–24852.
- Fairall, C., Bradley, E.F., Hare, J., Grachev, A., Edson, J., 2003. Bulk parameterization of air-sea fluxes: updates and verification for the COARE algorithm. *J. Clim.* 16 (4), 571–591.
- Farris, A., Wimbush, M., 1996. Wind-induced Kuroshio intrusion into the South China Sea. *J. Oceanogr.* 52 (6), 771–784.
- Gan, J., Allen, J.S., 2005. On open boundary conditions for a limited-area coastal model off Oregon. Part 1: Response to idealized wind forcing. *Ocean Model.* 8 (1), 115–133.
- Gan, J., Liu, Z., Hui, C.R., 2016a. A three-layer alternating spinning circulation in the South China Sea. *J. Phys. Oceanogr.* 46 (8), 2309–2315.
- Gan, J., Liu, Z., Liang, L., 2016b. Numerical modeling of intrinsically and extrinsically forced seasonal circulation in the China Seas: a kinematic study. *J. Geophys. Res. Oceans* 121 (7), 4697–4715.
- Gordon, A.L., 1986. Inter-ocean exchange of thermocline water. *J. Geophys. Res. Oceans* 91 (C4), 5037–5046.
- Gu, D., Philander, S.G., 1997. Interdecadal climate fluctuations that depend on exchanges between the tropics and extratropics. *Science* 275 (5301), 805–807.
- Hu, D., Cui, M., 1989. The western boundary current in the far-western Pacific Ocean, paper presented at Proceedings of Western International Meeting and Workshop on TOGA COARE, Inst. Fr. de Rech. Sci. pour le Dév. en Coop. Nouméa.
- Hu, D., Cui, M., Qu, T., Li, Y., 1991. A subsurface northward current off Mindanao identified by dynamic calculation. In: Elsevier oceanography series, edited, Elsevier, pp. 359–365.
- Hu, D., Hu, S., Wu, L., Li, L., Zhang, L., Diao, X., Chen, Z., Li, Y., Wang, F., Yuan, D., 2013. Direct measurements of the Luzon Undercurrent. *J. Phys. Oceanogr.* 43 (7), 1417–1425.
- Hu, D., Wu, L., Cai, W., Gupta, A.S., Ganachaud, A., Qiu, B., Gordon, A.L., Lin, X., Chen, Z., Hu, S., Wang, G., Wang, Q., Sprintall, J., Qu, T., Kashino, Y., Wang, F., Kessler, W.S., 2015. Pacific western boundary currents and their roles in climate. *Nature* 522 (7556), 299–308.
- Jensen, T.G., 2011. Bifurcation of the Pacific North Equatorial Current in a wind-driven model: response to climatological winds. *Ocean Dyn.* 61 (9), 1329–1344.
- Kashino, Y., España, N., Syamsudin, F., Richards, K.J., Jensen, T., Dutrieux, P., Ishida, A., 2009. Observations of the North Equatorial current, Mindanao current, and Kuroshio current system during the 2006/07 El Niño and 2007/08 La Niña. *J. Oceanogr.* 65 (3), 325–333.
- Kashino, Y., Ishida, A., Kuroda, Y., 2005. Variability of the Mindanao Current: Mooring observation results. *Geophys. Res. Lett.* 32 (18), n/a–n/a.
- Kim, Y.Y., Qu, T., Jensen, T., Miyama, T., Mitsudera, H., Kang, H.-W., Ishida, A., 2004. Seasonal and interannual variations of the North Equatorial Current bifurcation in a high-resolution OGCM: NEC BIFURCATION IN AN OGCM. *J. Geophys. Res.* 109 (C3).
- Li, J., Gan, J., 2020. On the formation dynamics of the North Equatorial Undercurrent. *J. Phys. Oceanogr.* (2020).
- Liu, X., and H. Zhou (2020), Seasonal variations of the North Equatorial Current across the Pacific Ocean. *J. Geophys. Res.: Oceans*, 125(6), e2019JC015895.
- Liu, Z., Gan, J., 2012. Variability of the Kuroshio in the East China Sea derived from satellite altimetry data. *Deep Sea Res. Part I* 59, 25–36.
- Liu, Z., Gan, J., 2016. Open boundary conditions for tidally and subtidally forced circulation in a limited-area coastal model using the Regional Ocean Modeling System (ROMS). *J. Geophys. Res. Oceans* 121 (8), 6184–6203.
- Liu, Z., Gan, J., 2017. Three-dimensional pathways of water masses in the South China Sea: A modeling study. *J. Geophys. Res. Oceans* 122 (7), 6039–6054.
- Mellor, G.L., Yamada, T., 1982. Development of a turbulence closure model for geophysical fluid problems. *Rev. Geophys. Space Phys.* 20 (4), 851–875.
- Nan, F., Xue, H., Yu, F., 2015. Kuroshio intrusion into the South China Sea: a review. *Prog. Oceanogr.* 137, 314–333.
- Nitani, H., 1972. On the deep and bottom waters in the Japan Sea. *Res. Hydrogr. Oceanogr.* 151–201.
- Qiu, B., Lukas, R., 1996. Seasonal and interannual variability of the North Equatorial Current, the Mindanao Current, and the Kuroshio along the Pacific western boundary. *J. Geophys. Res. Oceans* 101 (C5), 12315–12330.
- Qiu, B., Rudnick, D.L., Chen, S., Kashino, Y., 2013. Quasi-stationary north equatorial undercurrent jets across the tropical north Pacific Ocean. *Geophys. Res. Lett.* 40 (10), 2183–2187.
- Qu, T., Chiang, T.-L., Wu, C.-R., Dutrieux, P., Hu, D., 2012. Mindanao Current/Undercurrent in an eddy-resolving GCM. *J. Geophys. Res. Oceans* 117 (C6), n/a–n/a.
- Qu, T., Lukas, R., 2003. The bifurcation of the North Equatorial Current in the Pacific. *J. Phys. Oceanogr.* 33 (1), 5–18.
- Qu, T., Mitsudera, H., Yamagata, T., 1998. On the western boundary currents in the Philippine Sea. *J. Geophys. Res.* 103 (C4), 7537–7548.
- Qu, T., Mitsudera, H., Yamagata, T., 1999. A climatology of the circulation and water mass distribution near the Philippine coast. *J. Phys. Oceanogr.* 29 (7), 1488–1505.
- Ren, Q., Li, Y., Wang, F., Song, L., Liu, C., Zhai, F., 2018. Seasonality of the Mindanao current/undercurrent system. *J. Geophys. Res. Oceans* 123 (2), 1105–1122.
- Sasaki, H., Nonaka, M., Masumoto, Y., Sasai, Y., Uehara, H., Sakuma, H., 2008. In: High Resolution Numerical Modelling of the Atmosphere and Ocean. Springer New York, New York, NY, pp. 157–185.
- Schönau, M.C., Rudnick, D.L., 2015. Glider observations of the North Equatorial Current in the western tropical Pacific. *J. Geophys. Res. Oceans* 120 (5), 3586–3605.
- Shechetkin, A.F., McWilliams, J.C., 2005. The regional oceanic modeling system (ROMS): a split-explicit, free-surface, topography-following-coordinate oceanic model. *Ocean Model.* 9 (4), 347–404.
- Sun, C., Xu, J., Liu, Z., Tong, M., Zhu, B., 2008. Application of Argo data in the analysis of water masses in the Northwest Pacific Ocean.
- Sverdrup, H.U., 1947. Wind-driven currents in a baroclinic ocean; with application to the equatorial currents of the eastern Pacific. *Proc. Natl. Acad. Sci.* 33 (11), 318–326.
- Tian, J., Yang, Q., Liang, X., Xie, L., Hu, D., Wang, F., Qu, T., 2006. Observation of Luzon Strait transport. *Geophys. Res. Lett.* 33 (19).
- Toole, J., Millard, R.C., Wang, Z., Pu, S., 1990. Observations of the Pacific north equatorial current bifurcation at the Philippine coast. *J. Phys. Oceanogr.* 20 (2), 307–318.
- Toole, J., Zou, E., Millard, R., 1988. On the circulation of the upper waters in the western equatorial Pacific Ocean. *Deep Sea Res. Part A Oceanogr. Res. Papers* 35 (9), 1451–1482.
- Tozuka, T., Kagimoto, T., Masumoto, Y., Yamagata, T., 2002. Simulated multiscale variations in the western tropical Pacific: the Mindanao Dome revisited. *J. Phys. Oceanogr.* 32 (5), 1338–1359.
- Wang, F., Zang, N., Li, Y., Hu, D., 2015. On the subsurface countercurrents in the Philippine Sea. *J. Geophys. Res. Oceans* 120 (1), 131–144.
- Yaremchuk, M., Qu, T., 2004. Seasonal variability of the large-scale currents near the coast of the Philippines. *J. Phys. Oceanogr.* 34 (4), 844–855.
- Zhai, F., Hu, D., Qu, T., 2013. Decadal variations of the North Equatorial Current in the Pacific at 137°E. *J. Geophys. Res. Oceans* 118 (10), 4989–5006.
- Zhang, L., Hu, D., Hu, S., Wang, F., Wang, F., Yuan, D., 2014. Mindanao current/undercurrent measured by a subsurface mooring. *J. Geophys. Res. Oceans* 119 (6), 3617–3628.
- Zhang, L., Wang, F.J., Wang, Q., Hu, S., Wang, F., Hu, D., 2017. Structure and Variability of the North Equatorial Current/Undercurrent from Mooring Measurements at 130°E in the Western Pacific. *Sci. Rep.* 7, 46310.